High-resolution Poynting Flux Statistics from the Swarm Mission: How Much is Being Underestimated at Larger Scales?

D. D. Billett[1], K. A. McWilliams[1], I. P. Pakhotin[2], J. K. Burchill[2], D. J. Knudsen[2]. C. J. Martin[1]

[1]Institute of Space and Atmospheric Studies, University of Saskatchewan, Saskatoon, SK, Canada
[2]Department of Physics and Astronomy, University of Calgary, Calgary, AB, Canada

Key Points:

- High-resolution Swarm satellite data is used to examine Poynting flux across various spatial scales statistically
- Poynting flux decreases significantly with increasing spatial scale, dropping faster at scales under 10km
- Area Integrated Poynting flux is 9-28% larger in the northern hemisphere than in the south

Corresponding author: D. D. Billett, daniel.billett@usask.ca

Abstract

Underestimation of the transfer of energy between the magnetosphere and ionosphere, the Poynting flux, is a persistent issue in space weather studies and the high-latitude ionospheric models. Thought to be due to the inability to resolve small-scale fluctuations of the ionospheric electric field, this underestimation could lead to significant further underestimations in parameters such as the thermospheric mass density and consequential satellite drag. Utilising 16 Hz ion velocity and magnetic field measurements from the Swarm satellite mission, we examine the observed Poynting flux due to electric field fluctuations on very small spatial scales (∼1 km), and then artificially smooth the data to increase the observed scale. We quantify the decrease of integrated Poynting flux, poleward of 60/-60 degrees geomagnetic latitude, with increasing spatial scale. The decrease can be underestimated by as much as 15% by increasing scale from 1 km to only 8.6 km, or 16 Hz to 2 Hz equivalent, with upward Poynting flux decreasing significantly faster. Our results thus point to a significant Alfvén wave driven component of the Poynting flux on kilometre scales. Additionally, we observe a northern hemisphere preference for increased Poynting flux, of which we examine its dependence on scale size and interplanetary magnetic field.

Plain Language Summary

At Earth's high-latitudes, energy from space weather enters the upper atmosphere (>100 km) and is deposited mostly as heat. This heat can have numerous knock-on effects on the atmosphere, such as causing the air density to increase, which poses a risk to satellites orbiting at the same altitude. It is thus very important to accurately quantify the energy that enters the atmosphere from space, but it has been found that a large proportion of the energy is released on very small spatial scales (on the order of kilometres). These scales are often difficult to measure due to resolution limitations of most instruments, however, the Swarm constellation of satellites are equipped with electric field instruments that can retrieve measurements 16 times per second (16 Hz), equivalent to observing spatial scales of around 1 km. In this study, we use nearly 7 years of high-resolution Swarm data to calculate the average space weather energy input, known as the Poynting flux, and investigate the effect of artificially smoothing out the data to simulate larger spatial scales. We find significant underestimations of Poynting flux at larger scales com-

pared to the smaller ones, which stresses the importance of small-scale measurements in estimating the space weather - atmosphere energy budget.

1 Introduction

The energy transfer rate between the magnetosphere and the ionosphere-thermosphere via field-aligned currents, known as the Poynting flux, quantifies the impact of space weather changes on the atmosphere of Earth. The magnetosphere-ionosphere-thermosphere (MIT) system at high-latitudes is strongly coupled ultimately as a result of Poynting flux transfer. Due to the ubiquitous impact of various Poynting flux conditions, it is perhaps the most significant measure of the MIT energy budget and thus important to measure accurately.

The Poynting flux along a field line can be considered as consisting of two components. First, the quasi-static/DC large-scale Poynting flux associated with the typical R1/R2 field-aligned current system (Iijima & Potemra, 1976), with a scale size of several hundreds of kilometres at ionospheric F-region altitudes. The second is Poynting flux fluctuations on small spatial scales, less than ten kilometres, which can include and can be dominated by Alfvénic/AC fluctuations of the electric field (Knudsen et al., 1992). Electric field variability on small spatial and temporal scales have been a consistent source of uncertainty in calculations of MIT energy transfer (Codrescu et al., 1995; Cousins & Shepherd, 2012), leading to significant underestimations in models and statistical studies (Matsuo & Richmond, 2008; Cosgrove & Codrescu, 2009).

Localised Poynting flux ($\mathbf{S}$) at ionospheric high-latitudes (upwards of 60 degrees in both hemispheres), caused by fluctuations in the electric field, is given by:

$$\mathbf{S} = -\frac{1}{\mu_0} \left(\delta\mathbf{E} \times \delta\mathbf{B}\right) \cdot \hat{B} \tag{1}$$

where $\delta\mathbf{E}$ is the electric field perturbation from the background, large scale plasma convection electric field. $\delta\mathbf{B}$ is the magnetic field perturbation from the terrestrial magnetic field as a result of field-aligned currents and μ_0 is the permeability of free space. $\hat{B}$ is the unit vector parallel to the magnetic field such that $\mathbf{S}$ is also field-aligned. Fluctuations in $\delta\mathbf{E}$ and $\delta\mathbf{B}$ are however typically almost entirely horizontal (in the plane of the ionosphere), resulting in the Poynting flux being essentially field-aligned regardless. With sufficiently high spatio-temporal resolution measurements of the electric field such that fluctuations on scales $<$10 km are observed, $\mathbf{S}$ in Equation 1 should represent the afore-

mentioned Alfvénic/small-scale Poynting flux. On larger (quasi-static) spatial scales, $\delta\mathbf{E}$ would represent variability of the large-scale plasma convection.

Estimations of the Poynting flux from spacecraft have been possible since the advent of on-board magnetometers and electric field instruments (e.g. Knudsen, 1990; Kelley et al., 1991; Gary et al., 1995; Olsson et al., 2004). Early Poynting flux estimations such as these could generally be considered as mostly quasi-static due to the coarse sampling of data and thus large spatial scale. Recently, a combination of SuperDARN and AMPERE (Chisham et al., 2007; Anderson et al., 2014) fitted electric and magnetic field data products has also produced statistical Poynting flux estimations (Billett et al., 2021, 2022), but these too are likely to a be quasi-static due to the global nature of the SuperDARN and AMPERE fits. As time has passed however, significant data coverage now exists across numerous spacecraft such that statistical studies of the Poynting flux have been made possible with a much higher cadence of measurements (Ivarsen et al., 2020; Knipp et al., 2021; Cosgrove et al., 2022). These studies have typically used the full electric field vector (rather than the perturbation), and/or have utilised measurements that capture electric field variability on spatial scales of approximately 10 km and upwards. Measurements on spatial scales this small are able to detect Alfvénic electric field fluctuations (Miles et al., 2018), but recently, a statistical analysis of kilometre scale Poynting flux has been made possible due to newly reprocessed very high-resolution ion velocity measurements from the Swarm satellite mission (Friis-Christensen et al., 2006; Knudsen et al., 2017; Lomidze et al., 2019).

In this study, we utilise high spatio-temporal resolution data from the Swarm mission to examine how estimations of Poynting flux vary with scale-size of the measurements. In line with the thought that the inability to capture the smaller scale electric field variability results in significant Poynting flux underestimations, we find that Poynting flux does indeed decrease as the observed scale becomes coarser (larger). We use a filtering technique to artificially downgrade the resolution of the high-resolution data. This decrease in Poynting flux is not linear with scale, and the Poynting flux magnitude has a significant dependence on the orientation of the interplanetary magnetic field (IMF). We also note and expand upon a hemispheric asymmetry, recently seen in other studies of the Poynting flux (Pakhotin et al., 2021; Knipp et al., 2021; Cosgrove et al., 2022). Our goal with this study is to quantify the level of underestimation that measurements at a larger spatial scale induce, conversely observing the "missing" Poynting flux that

very small-scale measurements can resolve. We make comparisons to previous statistical studies as to the morphology and magnitude of the Poynting flux, discussing the implication of what results may be considered "Alfvénic" or "quasi-static" driven.

2 Swarm Data Processing

Swarm A and B are part of the Swarm constellation of satellites (also including Swarm C and E, not utilised in this study) which operate in near-polar orbits at altitudes of ∼460 km and ∼510 km, respectively. A 16 Hz Poynting flux product is derived with equation 1, using a combination of ion velocity ($\mathbf{v}$) and magnetic field ($\mathbf{B}$) measurements from both satellites. First, the electric field, $\mathbf{E}$, is calculated using $\mathbf{E} = -\mathbf{v} \times \mathbf{B}$. The ion velocity is obtained at 16 Hz from the Swarm Thermal Ion Imager (TII) instruments (Knudsen et al., 2017; Lomidze et al., 2019). A 16 Hz magnetic field product is derived by downsampling the 50 Hz $\mathbf{B}$ measurements from the onboard magnetometer (Leger et al., 2009). Electric field components in the x, y and z directions (satellite along-track in the direction of motion, cross-track to the right and vertically downward towards Earth, respectively) are determined for $\mathbf{v}$ measurements from both the horizontal and vertical sensors on the TII instrument, which are then averaged into a single component for the purpose of this study.

To calculate the Poynting flux using Equation 1, the large-scale convection electric field and terrestrial magnetic field must be removed from the Swarm $\mathbf{E}$ and $\mathbf{B}$ data. We apply the same method of determining the "background" fields as that used in Ivarsen et al. (2020), i.e., by using a second-order Savitsky-Golay low-pass (SGLP) filter of 225 s in width. Using a long SGLP filter such as this has the added benefit of extracting large-scale offsets present in the data that is not of geophysical origin (Koustov et al., 2019). Subtracting the background fields yields the perturbation electric ($\delta\mathbf{E}$) and magnetic ($\delta\mathbf{B}$) fields, which are then rotated from the satellite-track coordinate system (x, y and z) into the mean field-aligned (MFA) frame. In this final coordinate system, z is along the direction of the magnetic field as determined by the SGLP filtered data, x is magnetically north and y is magnetically east. The background field removal and MFA rotation described here is broadly similar to that used in other studies which have examined Poynting fluxes from the Swarm mission (e.g. Park et al., 2017; Pakhotin et al., 2021). As perturbations in the magnetic field, $\delta\mathbf{B}$, are almost entirely horizontal, the full Poynting flux vector ($\mathbf{S}$) is essentially field-aligned (parallel to $\hat{B}$), in the MFA z direction.

We calculate the Poynting flux from Swarm A and B data from December 11th, 2013 through November 30th, 2020, utilising the quality and calibration flags described by the "Swarm Level 1b Product Definition" (available at `https://earth.esa.int/eogateway/missions/swarm/product-data-handbook/`) and the "EFI TII Cross-Track Flow Data Release Notes" (available in Swarm data repository, link provided in acknowledgements). We only utilise "good data" as indicated by these flags, which are driven by various criterions such as a maximum velocity (8 km/s) and minimum latitude threshold. For this study, we impose a stricter low-latitude threshold of 60 degrees latitude in Altitude-adjusted corrected geomagnetic coordinates (AACGM; Shepherd, 2014) to remove mid-latitude and equatorial phenomena. Calculated 16 Hz Poynting fluxes are sorted and averaged into equal area grids upwards of 60 degrees AACGM latitude (henceforth referred to as MLat), where each cell is 1 degree of MLat tall and has an increasing AACGM longitudinal (MLon) width as they approach the poles. Downward (into to ionosphere) and upward (out of) Poynting fluxes are sorted and averaged separately. Poynting fluxes from both Swarm A and B are also combined into the same statistical patterns for this study, as the altitude difference between the satellites will result in a negligible difference in Poynting flux along the same magnetic field-line. This is because the Poynting flux is almost entirely dissipated as Joule heating at a lower altitude than the spacecraft, in the E-region, where the Pedersen conductivity is highest (Deng et al., 2011).

The Poynting flux sorting is done in categories based on the orientation of the IMF in geocentric solar magnetospheric (GSM) coordinates. IMF sorting is carried out using the "clock-angle", i.e. the angle the IMF vector makes with the B_z positive axis in the B_y-B_z plane, to sort into 8 equally sized sectors of 45° in width. The first sector is centred on clock angles of -22.5 to +22.5°, or "northward IMF", and so on. We additionally sort the data into separate northern and southern hemisphere categories. The combined coverage of the Swarm A and B satellites in the northern and southern hemispheres are shown in Figures 1 and 2, respectively, in terms of the number of 16 Hz data points falling into each grid cell. The plots are polar projections in MLat-Magnetic Local Time (MLT) coordinates, sorted into the aforementioned IMF categories and show the occurrence of downward (into the ionosphere) Poynting fluxes only. The occurrence rate of upward Poynting fluxes are significantly lower, but they have a spatial distribution that is close to Figures 1 and 2. Due to the low occurrences when binned this way, we do not show average distributions of upward Poynting flux in this manuscript. We

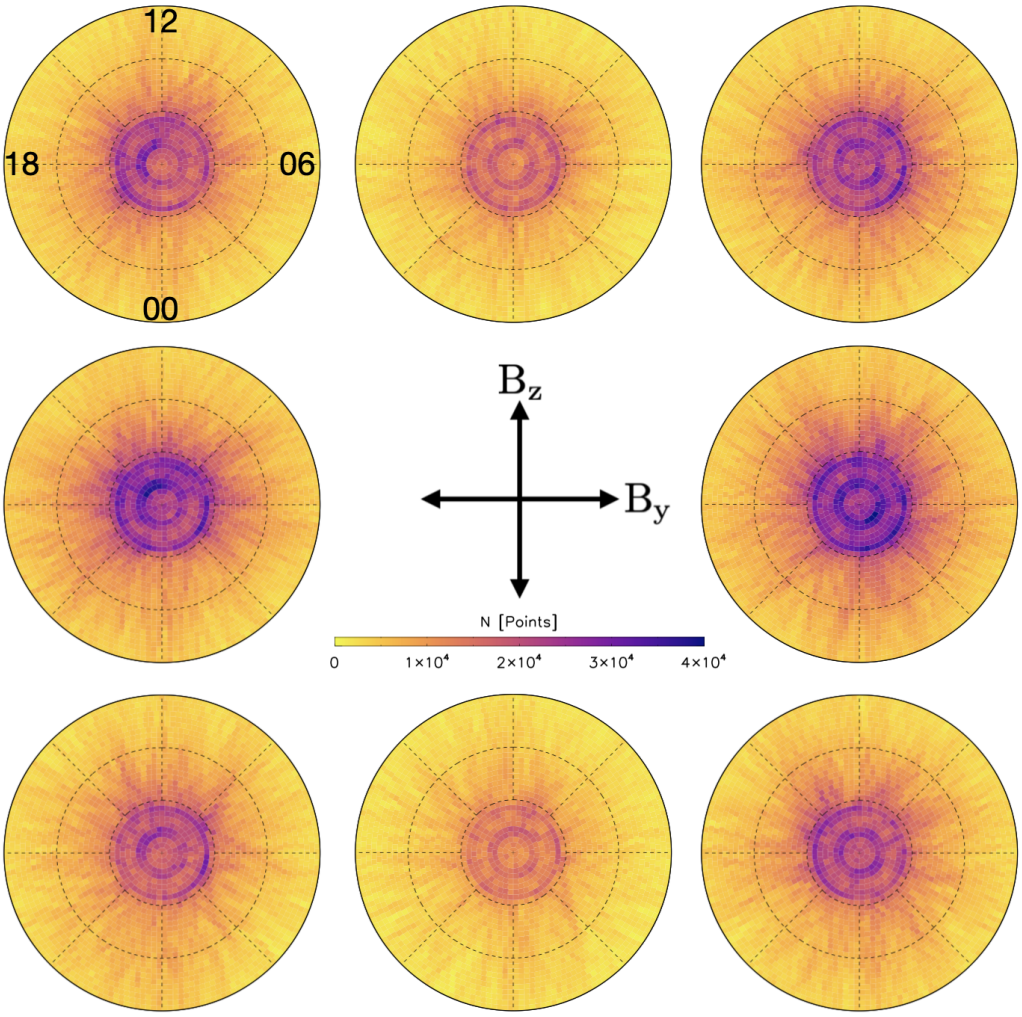

Figure 1. Distributions of the total number of samples of the combined Swarm A and B 16 Hz datasets in the northern hemisphere, between December 2013 and November 2020. Plots are sorted by IMF clock angle orientation, given by the axis in the centre. The projection is polar, and the coordinate system in Mlat-MLT in AACGM. Concentric circles separate 10° of AACGM latitude, down to a minimum of 60°. Magnetic local midnight (00 hrs) is orientated at the bottom of each plot, dawn (06 hrs) to the right, noon (12 hrs) at the top and dusk (18 hrs) to the left.

do however, towards the end of the paper, show hemispherically integrated values of upward Poynting flux in a different format, as it is significantly less "noisy" and less affected by one-off events. Statistical patterns of Swarm derived upward Poynting flux, not sorted by the IMF orientation, can be found in Ivarsen et al. (2020).

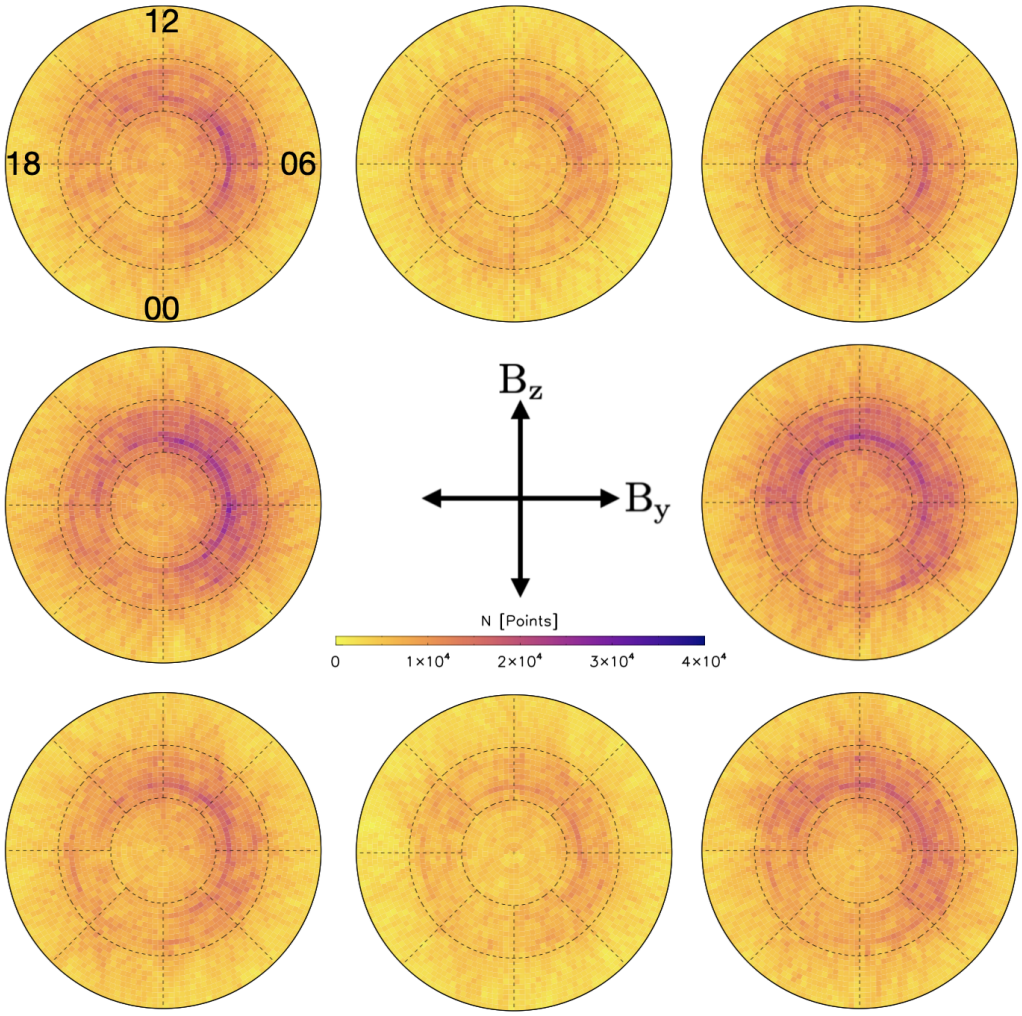

Figure 2. Same format as Figure 1, but for the southern hemisphere Swarm A and B distributions.

We note that because the Swarm satellites have a near-polar inclination in geographic coordinates, the southern hemisphere data coverage in a magnetic frame (Figure 2) is much more diffuse than the northern hemisphere equivalent (Figure 1). This is due to the AACGM pole being much closer to the geographic pole in the northern hemisphere versus the south, leading to the "donut" shaped coverage in the south. We also note that the occurrence rate of clock-angles in the purely northward and purely southward B_z categories (middle top and middle bottom plots in Figures 1 and 2) is lower than the others, which is likely due to the typical orientation of the unperturbed Parker spiral as it reaches Earth (i.e., mostly azimuthal in the B_y-B_z plane).

To examine the effects of various scale-sizes on the calculation of Poynting flux, we derive several additional Poynting flux datasets from the 16 Hz Swarm **E** and **B** measurements by imposing a series of increasing SGLP filters. This is a very similar process to that carried out by Pakhotin et al. (2021), who derived SGLP filters for the 2 Hz Swarm A TII dataset. We produce 13 SGLP filtered Poynting flux datasets in total, using half-window sizes (points either side of a 16 Hz measurement) of 2, 4, 8, 16, 32, 64, 80, 160, 240, 320, 400, 480 and 560. The SGLP full windows thus range from 0.3125 s to 70.0625 s in time, or assuming a satellite orbital velocity of 7.6 km/s, 2.375 km to 532.475 km in distance. Taking into account the Nyquist criterion (i.e. observed scales are half of the sampling frequency), the distances covered by the SGLP filters represent variability on scales of approximately 4.75 km to 1064.95 km. We consider these filtered datasets as a proxy for "true" measurements across those scales. For example, a 4 data-point half-window (9 points in total, including the centre point) is 0.56 s long and captures variability on scales of ∼8.55 km, which is approximately equivalent to the commonly used Swarm Electric Field Instrument (EFI) 2 Hz data product. The unfiltered 16 Hz Poynting flux by contrast captures scales of 0.95 km or greater, allowing for the analysis of kilometre-scale variability.

Figure 3 illustrates the data processing scheme for a northern hemisphere auroral zone pass of Swarm A. Positional information of the satellite is given in Figure 3[a], showing that the pass was roughly a latitudinal slice in the post-midnight sector. Panels [b] and [c] of Figure 3 show the meridional (north-south) component of $\delta\mathbf{E}$ and $\delta\mathbf{B}$, for the unfiltered 16 Hz data along with three SGLP filters of sizes shown in the key at the bottom. The electric field perturbation data is much more variable than that of the magnetic field, indicating that most of the Poynting flux variability is driven by the TII ion velocity data. Increasing SGLP filter sizes effectively "smooths-out" both $\delta\mathbf{E}$ and $\delta\mathbf{B}$ by removing higher frequencies of variability. Panel [d] shows the field-aligned Poynting flux calculated from the data in [b] and [c] (as well as from the zonal components, not shown). Finally, panel [e] shows the evolving Poynting energy derived by continuously integrating the Poynting flux in [d] (units of millijoules per metre squared). Figure 3[e] illustrates that with increasing filter size, mimicking measurements made on increasing scale sizes, less total energy as Poynting flux is captured by the measurements. As also shown by Pakhotin et al. (2021), this energy discrepancy illustrates that small-scale perturbations

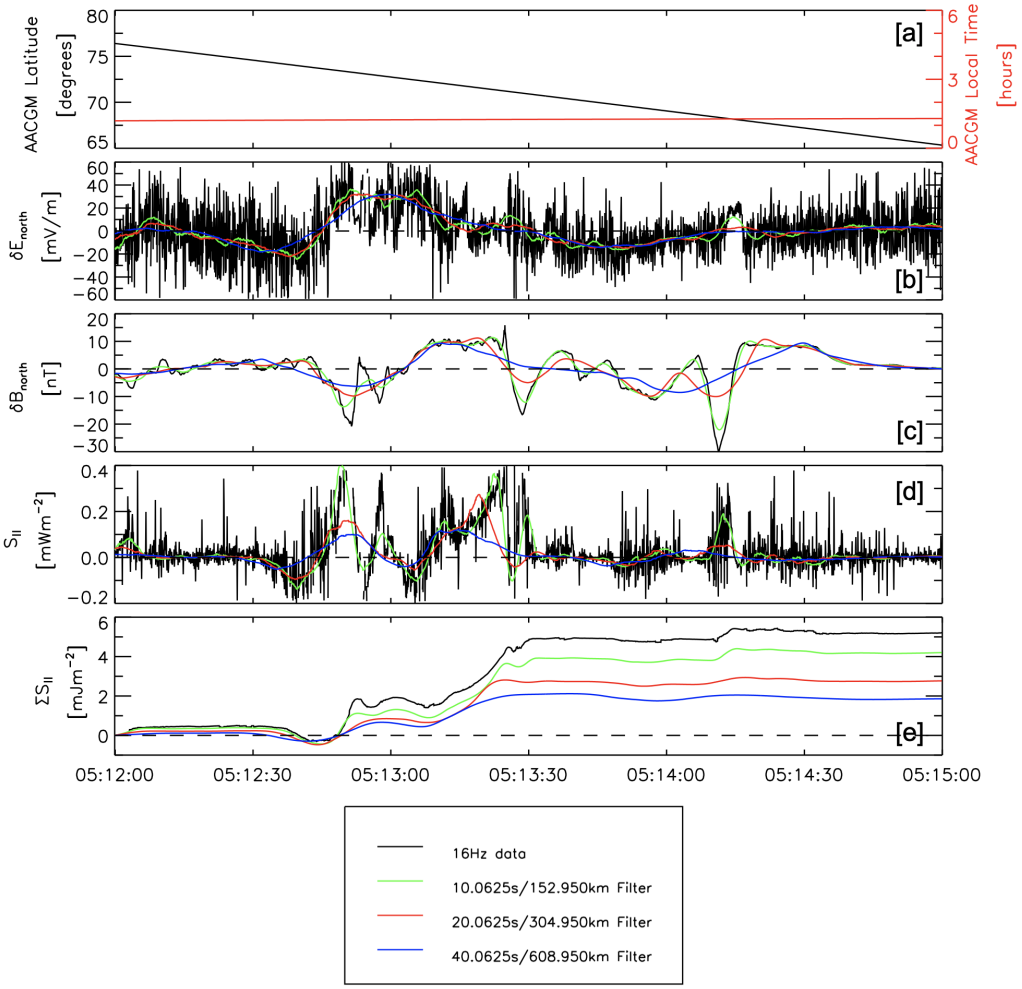

Figure 3. Example Swarm A pass of the northern hemisphere auroral region on 17th November 2016, which was also shown in Pakhotin et al. (2021). Illustrated is the effect of various SGLP filters applied to the 16 Hz electric/magnetic field data and the resulting Poynting flux. [a]: AACGM positional information for Swarm A. [b]: Meridional perturbation electric field. [c]: Meridional perturbation magnetic field. [d]: Poynting flux. [e]: Poynting energy derived from the Poynting flux in [d] by continuously integrating in time. Colours on [b]-[e] denote the unfiltered 16 Hz data product in black, then SGLP filters of approximately 10 s, 20 s and 40 s for green, red and blue respectively. The corresponding filter scale sizes (Nyquist) are also shown, assuming a satellite orbital velocity of 7.6 km/s.

of the ionospheric electric field can account for a significant proportion of the electromagnetic energy deposited in the high-latitude atmosphere.

3 Results and Discussion

Results and discussion in this section are divided into two subsections, both of which assess the impact of increasing SGLP filter sizes on the Swarm derived statistical Poynting fluxes. Section 3.1 will focus on asymmetries due to the orientation of the IMF and only include results from the northern hemisphere. Section 3.2 will investigate hemispheric differences in the spatial distribution of Poynting flux, as well differences in integrated Poynting flux.

3.1 Solar Wind

Statistical patterns of the Swarm derived northern hemisphere downward Poynting flux are shown in Figure 4, for the unfiltered 16 Hz dataset. Enhancements are consistently highest on the dayside, centred on magnetic local noon for $B_y < 0$ orientations, but pre-noon for $B_y = 0$ and $B_y > 0$. This region is roughly associated with the dayside cusp, and its B_y asymmetry is consistent with the dawnside "skew" seen in numerous models of the ionospheric convection electric potential (e.g. Ruohoniemi & Greenwald, 1996; Weimer, 2005; Förster & Haaland, 2015; Thomas & Shepherd, 2018). The consistent nightside Poynting flux enhancements are also skewed, but towards the duskside pre-midnight sector. These two primary enhancement regions, on the dayside and nightside, bear a strong resemblance to the locations of highest electric field variability statistically (Matsuo & Richmond, 2008). As the Poynting flux is strongly dependent on the electric field variability (e.g. in Figure 3), this result is perhaps not unexpected. During southward IMF orientations (bottom three plots of Figure 4), the Poynting flux is generally more enhanced across all local times, especially for the purely southward orientation. This implies that convection electric field variability is more ubiquitous during active solar wind driving conditions.

The electric field variability in the aforementioned dayside and nightside regions are associated with Alfvén waves, with the Poynting flux in Figure 4 additionally aligning well with the Alfveń wave occurrence rate and the consequential "Alfvénic oval" (Chaston et al., 2007; Hatch et al., 2017; Keiling, 2021). The Swarm derived Poynting flux in turn closely resembles the average "Alfveńic Poynting flux", which has previously been derived by applying bandpass filters to retain only Alfvénic frequencies of electric field variability (Keiling et al., 2003; Zhang et al., 2014). We thus infer that the unfiltered Swarm

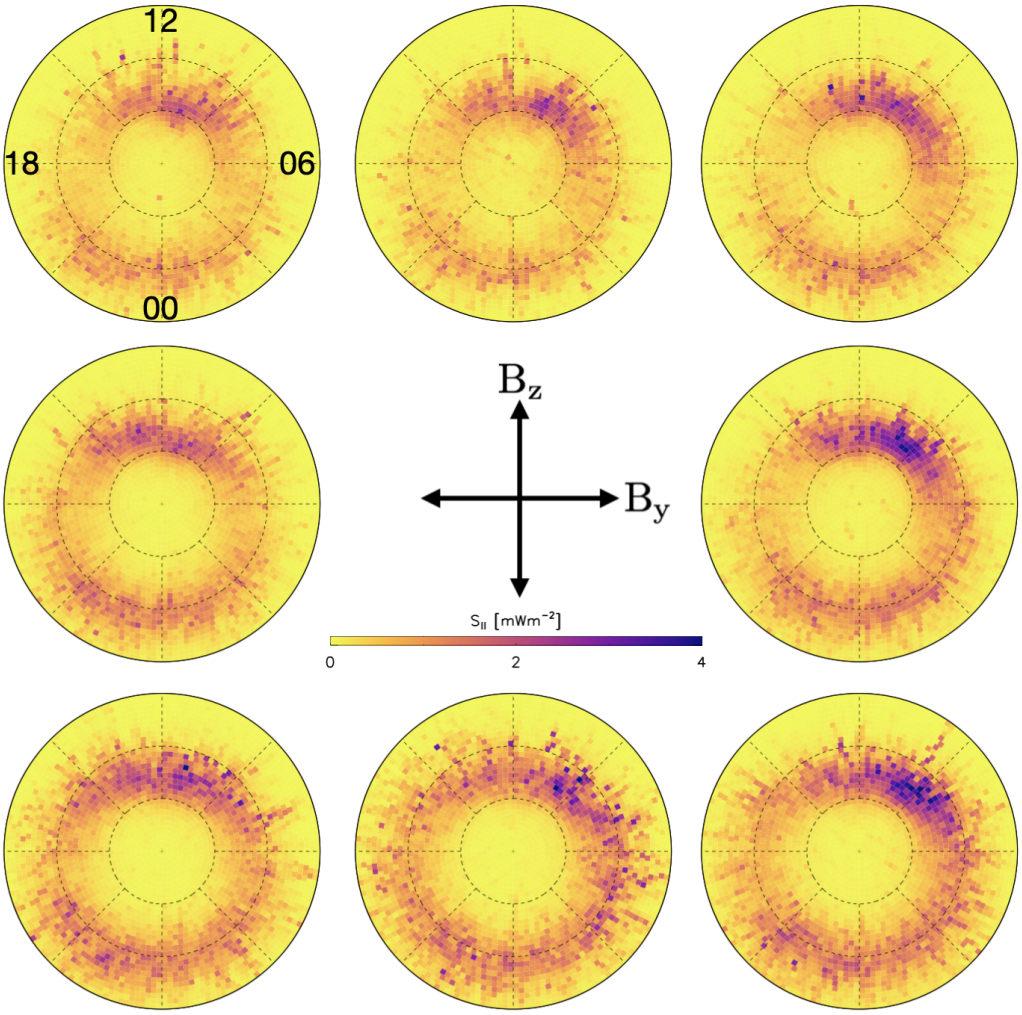

Figure 4. Statistical patterns of downward Poynting flux, sorted by IMF orientation, derived from the combined Swarm A and B 16 Hz datasets. Coordinates are in Mlat-MLT, as in Figure 1 and 2.

measurements at 16 Hz are observing small-scale fluctuations due to Alfvén waves, driving small-scale or "AC" Poynting flux (Knudsen et al., 1992). Poynting flux on this scale is further associated with neutral mass density enhancements in the thermospheric cusp region (Lotko & Zhang, 2018; Hogan et al., 2020; Billett et al., 2021).

A prominent cusp Poynting flux enhancement, such as those seen in Figure 3, has previously been seen in statistics from the FAST and DMSP spacecraft (Cosgrove et al., 2014; Knipp et al., 2021) under all IMF orientations. These studies calculated the Poynting flux using the full electric field vector (**E**) rather than its perturbation from the back-

ground large-scale convection ($\delta\mathbf{E}$), therefore representing the large-scale quasi-static Poynting flux better than the Alfvénic. However, the quasi-static Poynting flux patterns derived from SuperDARN electric fields and AMPERE magnetic fields by Billett et al. (2022) show a much lower magnitude cusp contribution, compared to those from Cosgrove et al. (2014) and Knipp et al. (2021). We suggest that the latter spacecraft observations may thus be observing some contributions from both quasi-static and Alfvénic Poynting flux, revealing the strong cusp enhancements also seen in our Swarm statistics. In fact, Knipp et al. (2021) do note that an observed hemispheric Poynting flux asymmetry (which we discuss further later) may be due to stronger field-aligned currents, as a result of "an extension of Alfvénic behaviour into what has previously been considered as the "quasi-static" regime". The Billett et al. (2022) SuperDARN/AMPERE statistics, by contrast, could be representing almost entirely the quasi-static Poynting flux. In this case, the discrepancy is likely due to the higher spatio-temporal resolution of the satellite electric field measurements (1 Hz for DMSP, and between 33 and 4 Hz for FAST) when compared to both SuperDARN and AMPERE, both of which utilise global scale fits to data averaged over several minutes. Essentially, this implies that the SuperDARN/AMPERE fitted electric and magnetic field products are not well suited to observing Alfvénic associated variability.

Imposing increasingly larger SGLP filters decreases the total measured integrated Poynting flux for the example event in Figure 3, due to the smoothing out of high-frequency electric and magnetic field variability. The decrease in Poynting flux with increasing scale size is also evident in statistical patterns of Swarm data, when substituting the original 16 Hz Swarm measurements with their filtered counterparts. This decrease is illustrated in Figure 5, for the pure northward IMF 16 Hz statistical pattern (top middle of Figure 4) and three of the SGLP filtered datasets. Plots in Figure 5 are dayside only and have been shown overlapping for ease of comparison. The total hemisphere integrated power (in gigawatts) for the corresponding statistical pattern is also displayed.

Figure 5 shows that with increasing SGLP filter size, the measured Poynting flux decreases at all local times, without the morphology changing significantly. This decrease is true for all IMF orientations. In the example, the largest shown filter size of around 40s (equivalent to a scale size of ∼609 km) results in a significant drop of the total hemisphere integrated Poynting flux to 8.65 GW, or around a 32.4% drop compared to 12.79 GW for the unfiltered 16 Hz data. The SuperDARN gridded electric field measurements by

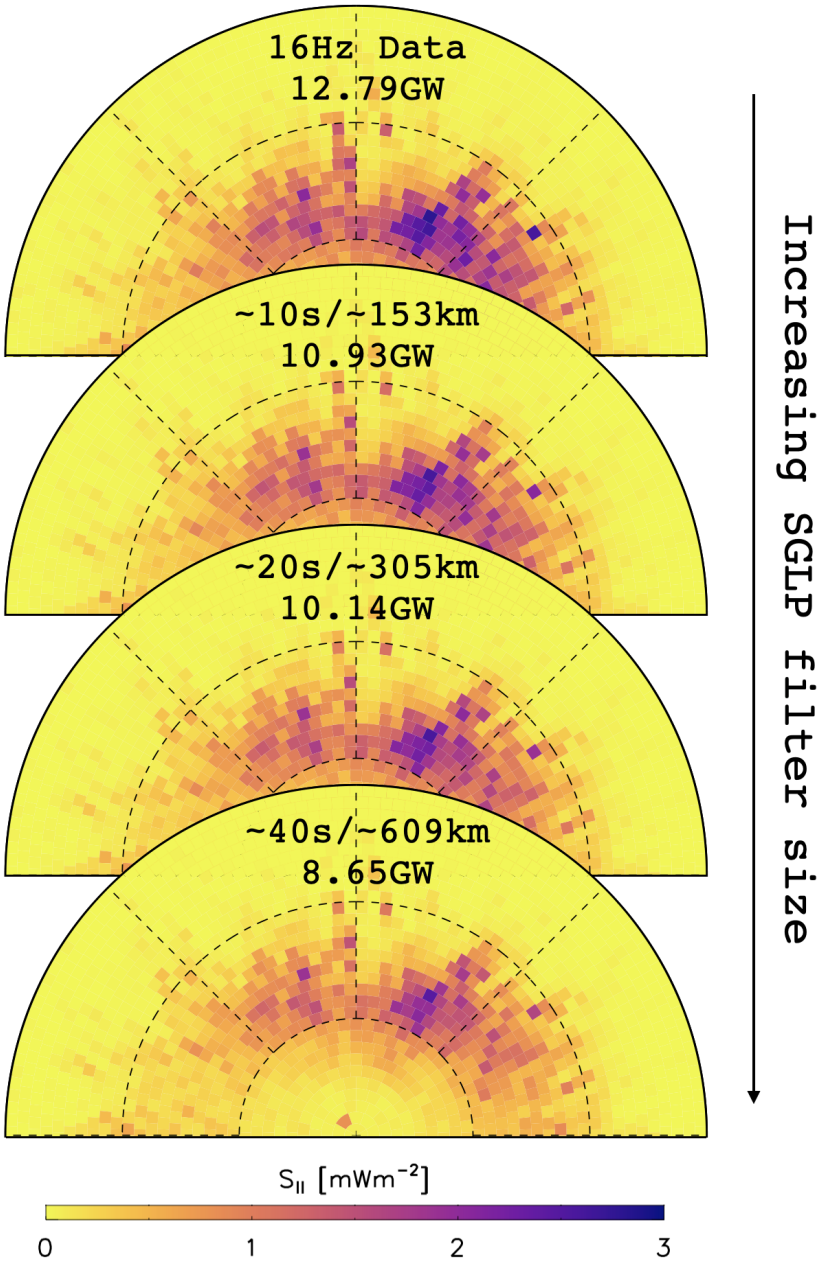

Figure 5. Dayside plots of the statistical downward Poynting flux in the northern hemisphere, for the IMF B_z northward category. From top to bottom, the statistics are derived from: the unfiltered Swarm A and B 16 Hz datasets, then the same dataset with SGLP filters of ~10s, ~20s and ~40s applied. These are the same filter scale sizes shown in Figure 3, with corresponding approximate scale sizes. The total hemispherically integrated Poynting flux power is also shown for each plot.

comparison have a spatial resolution of around 115 km, which for the SGLP equivalent lies slightly below the 10 s filter, or a 15.5% integrated Poynting flux drop. There is thus the potential for electric field instruments with a similar or larger spatial resolution than the SuperDARN to significantly underestimate the impact of electric field variability on the resulting Poynting flux. In the dayside cusp region, where the Poynting flux measured by Swarm is largest in statistics, the underestimation at large SGLP filters is particularly stark.

To quantitatively compare the amount of Poynting flux flowing into or out of the ionosphere at various SGLP filter sizes, we calculate the total area integrated flux (hemispheric power) for each Swarm statistical pattern, including for the upward flux averages. The results of this comparison are shown in Figure 6[a]. Colour and symbols on each line represent IMF orientation, solid lines are downward Poynting flux and dashed lines are upward. A filter window of 0 s denotes the hemispheric power of the unfiltered 16 Hz dataset. The largest magnitudes of hemispheric power are consistently from the statistical averages of southward IMF orientations (red circles, pink hourglasses and purple bowties), for both downward and upward Poynting fluxes. Conversely, the lowest magnitudes of hemispheric power are from northward IMF orientations (yellow triangles, green diamonds and mauve stars).

For the unfiltered 16 Hz and first few SGLP filtered datasets, the average downward integrated Poynting flux is roughly 2.5 times larger than the equivalent upward for all IMF orientations. These results are consistent with the dominance of magnetospheric forcing to the ionosphere rather than vice versa (as a potential result of the neutral wind dynamo; Kelley et al., 1991), and with previous studies who observed lower magnitude upward Poynting fluxes statistically (e.g. Gary et al., 1995; Keiling et al., 2003; Ivarsen et al., 2020). At large SGLP filters (e.g. 40+ s/600+ km), the downward integrated Poynting flux is closer to 3 times larger than the upward for all IMF orientations. This difference implies that upward Poynting flux drops off slightly faster than downward flux with increasing observation scale size.

The total hemispheric power for all for all curves in Figure 6[a] drops faster at the smaller SGLP filters (0.31-4.06 s/4.75-61.75 km) versus the larger filters, where the decrease becomes almost linear. In Figure 6[b], the results of [a] are shown in terms of percentage of the original unfiltered 16 Hz dataset, which emphasises the aforementioned

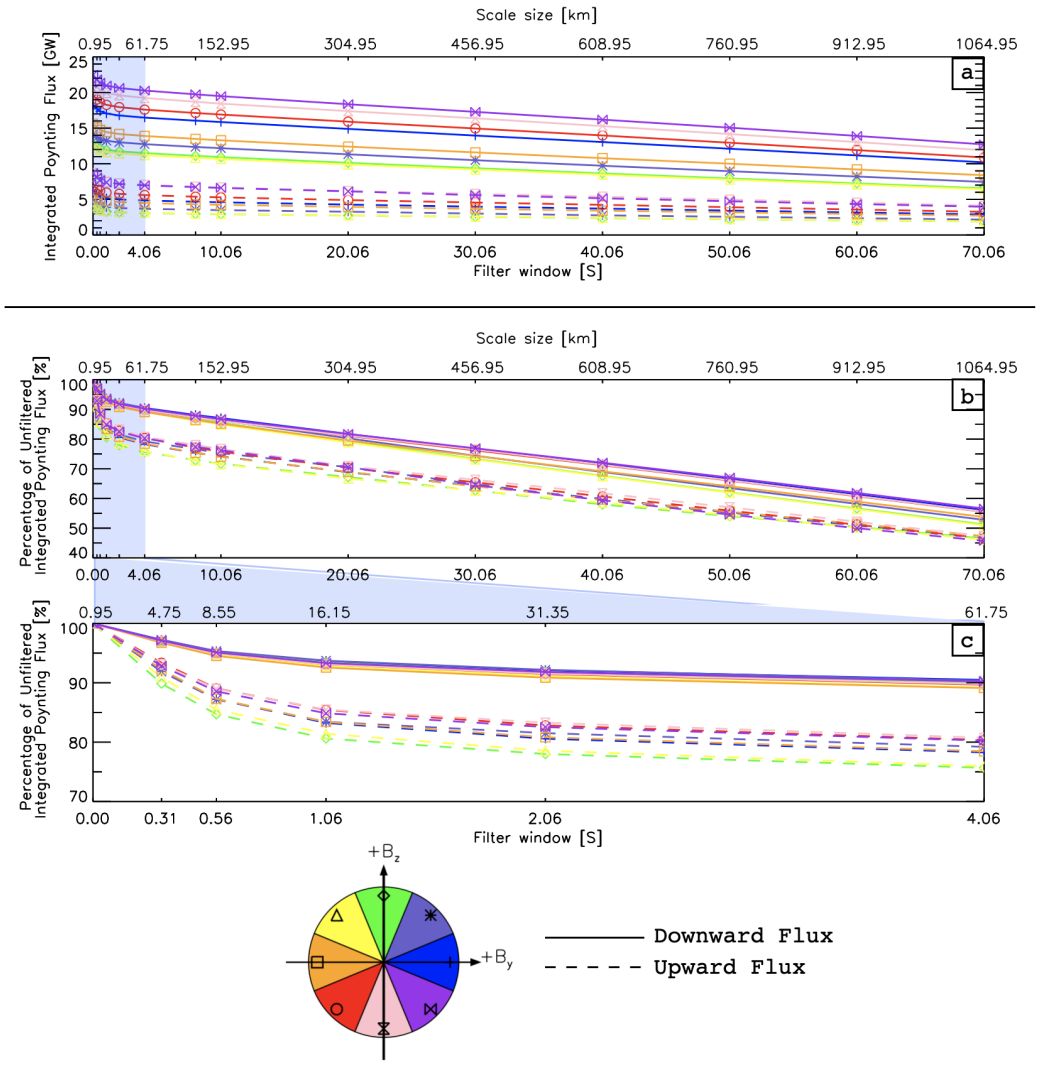

Figure 6. Comparison of the northern hemisphere integrated Poynting flux (total hemispheric power) with increasing SGLP filter size. Colour and symbols represent IMF orientation. Solid and dashes lines represent downward (into) and upward (out of) the ionosphere, respectively. [a]: Absolute Poynting flux power. [b]: Power as a percentage of unfiltered 16 Hz dataset (i.e. filter window = 0 s). [c]: Zoomed in version of [b]. The highlighted region in [a] and [b] correspond to the filters shown in [c].

hemispheric power decrease. Figure 6[c] in turn shows a zoomed in version of Figure 6[b], showing only SGLP filters in the range of 0.31-4.06 s/4.75-61.75 km. At the largest SGLP filter of 70.06 s/1064.95 km, the hemispheric powers are 51-57% and 46-48% of the unfiltered 16 Hz value for downward and upward flux, respectively, depending on IMF orientation.

The SGLP filter of 0.56 s/8.55 km applied to the 16 Hz Swarm data could be considered analogous to the commonly used 2 Hz EFI dataset, as the spatial scales observed are close and the 2 Hz data is simply downsampled from the 16 Hz. For downward Poynting flux, the decrease of hemispheric power at the 0.56 s filter is between 4 and 5% depending on IMF orientation. For upward Poynting flux, the decrease is between 11 and 15%. These are both significant drops considering the relatively small increase of observed spatial scale from 0.95 km to 8.55 km, and also shows that upward Poynting flux drops faster at very small spatial scales than downward Poynting flux. We consider this further evidence for a significant Alfvén wave driven component of electric field variability at frequencies above 2 Hz, which was also seen by Miles et al. (2018) in their analysis of Swarm data during a discrete auroral arc event and by Pakhotin et al. (2018) during northward IMF conditions. These fine scales are on the same order as intense field-aligned currents initially observed by Lühr et al. (2004) in association with thermospheric density upwelling in the cusp, which have been shown to be highly variable compared to the large-scale quasi-static system (Lühr et al., 2015). Our results further imply that Alfvén waves have a significantly larger impact on the average magnitude of upward Poynting flux, versus downward.

3.2 Hemispheric Asymmetry

Figure 7 shows the Swarm unfiltered 16 Hz statistical downward Poynting fluxes, sorted by IMF, for the southern hemisphere. When compared to the northern hemisphere equivalent patterns (Figure 4), there are notably lower magnitudes, in particular on the dayside. The regions of enhancement are somewhat similar: distinct dayside and nightside enhancements, with more local times seeing enhanced Poynting flux under purely southward IMF. However, the location of the dayside enhancement region is more symmetric around magnetic local noon, particular when $B_y > 0$. This is consistent with hemispheric asymmetries of the ionospheric convection electric field (Cousins & Shepherd, 2010; Pettigrew et al., 2010; Förster & Haaland, 2015), which is ultimately driven by drastically different ionospheric conductivity conditions in the two hemispheres under varying dipole tilt angles.

To examine the spatial asymmetries in the northern and southern hemisphere Poynting fluxes further, Figure 8 shows difference plots of Figures 4 and 7 (southern hemisphere downward flux subtracted from the northern). In most regions in Figure 8, the statis-

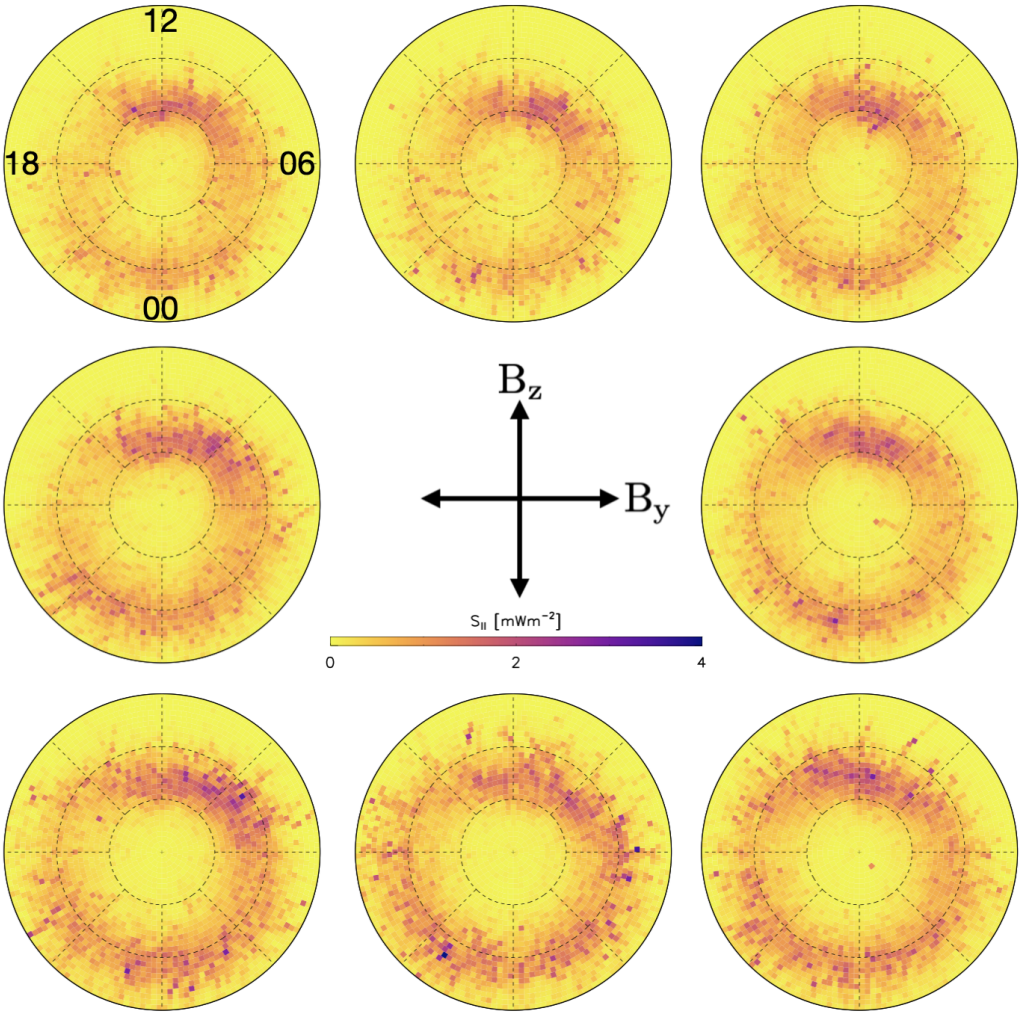

Figure 7. Same as Figure 4, but for the southern hemisphere statistical 16 Hz Poynting flux.

tical northern hemisphere downward Poynting flux is greater than in the south. This northern hemisphere preference is particularly emphasised in the dayside pre-noon sector, most prominently for IMF $B_y > 0$. On the nightside, by contrast, the difference in the northern and southern hemisphere Poynting flux is less significant. Regions where Poynting flux in the southern is noticeably larger are pre-noon when the IMF B_y is negative, and post-noon when B_y is positive. This combined dayside region is where the greatest B_y asymmetry in Figures 4 and 7 exists, which as mentioned previously, is likely because of convection electric field asymmetries. This additionally implies a similar B_y asymmetry in the Alfvénic oval (Keiling, 2021), i.e. in the occurrence rate of Alfvén waves.

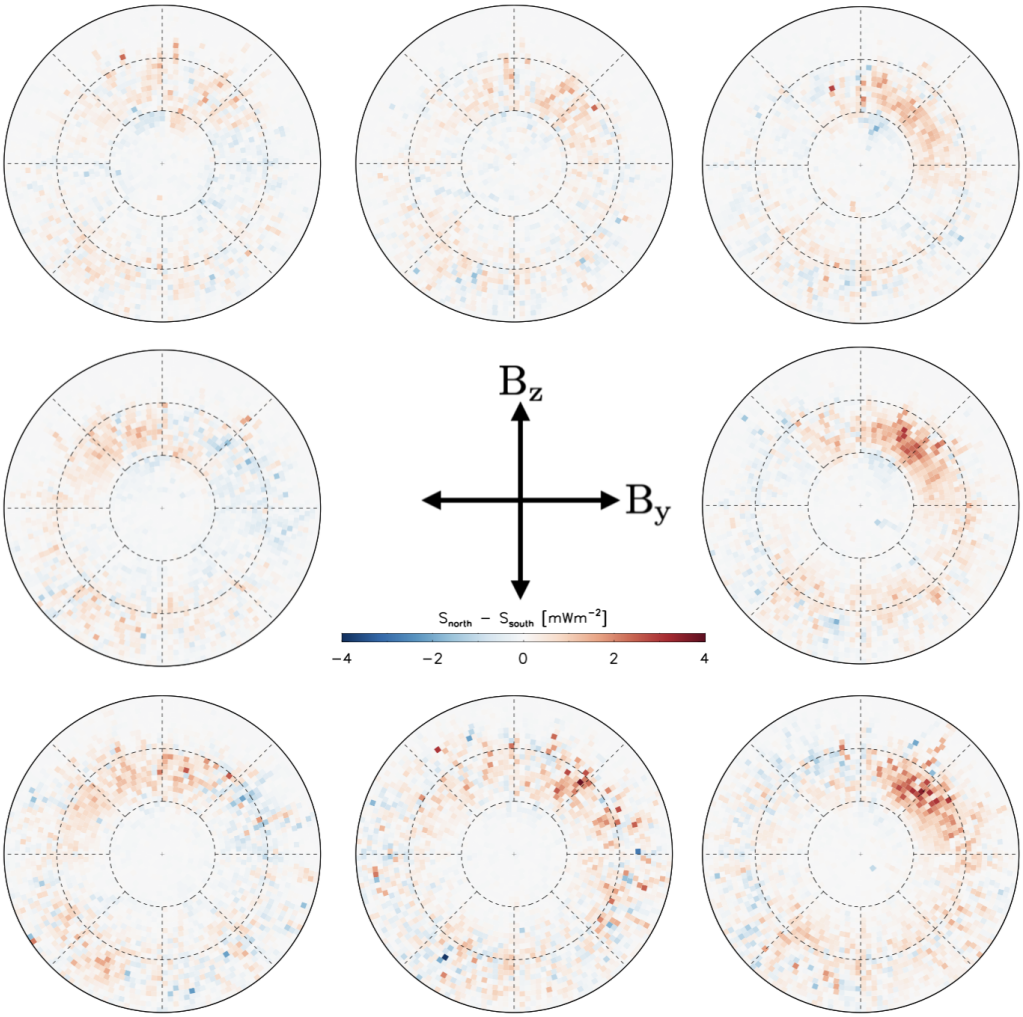

Figure 8. Difference plots of the northern and southern hemisphere Poynting fluxes shown in Figures 4 and 7. Positive values indicate stronger Poynting flux in the northern hemisphere, and vice versa.

Recently, studies have noted the hemispheric asymmetry of Poynting flux and seen that there is a clear preference for more energy input into the northern hemisphere (Pakhotin et al., 2021; Knipp et al., 2021; Cosgrove et al., 2022). This holds true for our Swarm statistics as well, with the northern hemisphere downward and upward integrated Poynting fluxes being significantly larger than those in the northern hemisphere. A full comparison of northern and southern hemisphere integrated values is shown in Figure 9[a] and [b], which are in the same format as Figure 6a, but showing the north-south difference in downward and upward magnitudes. Positive values mean a greater hemispheric

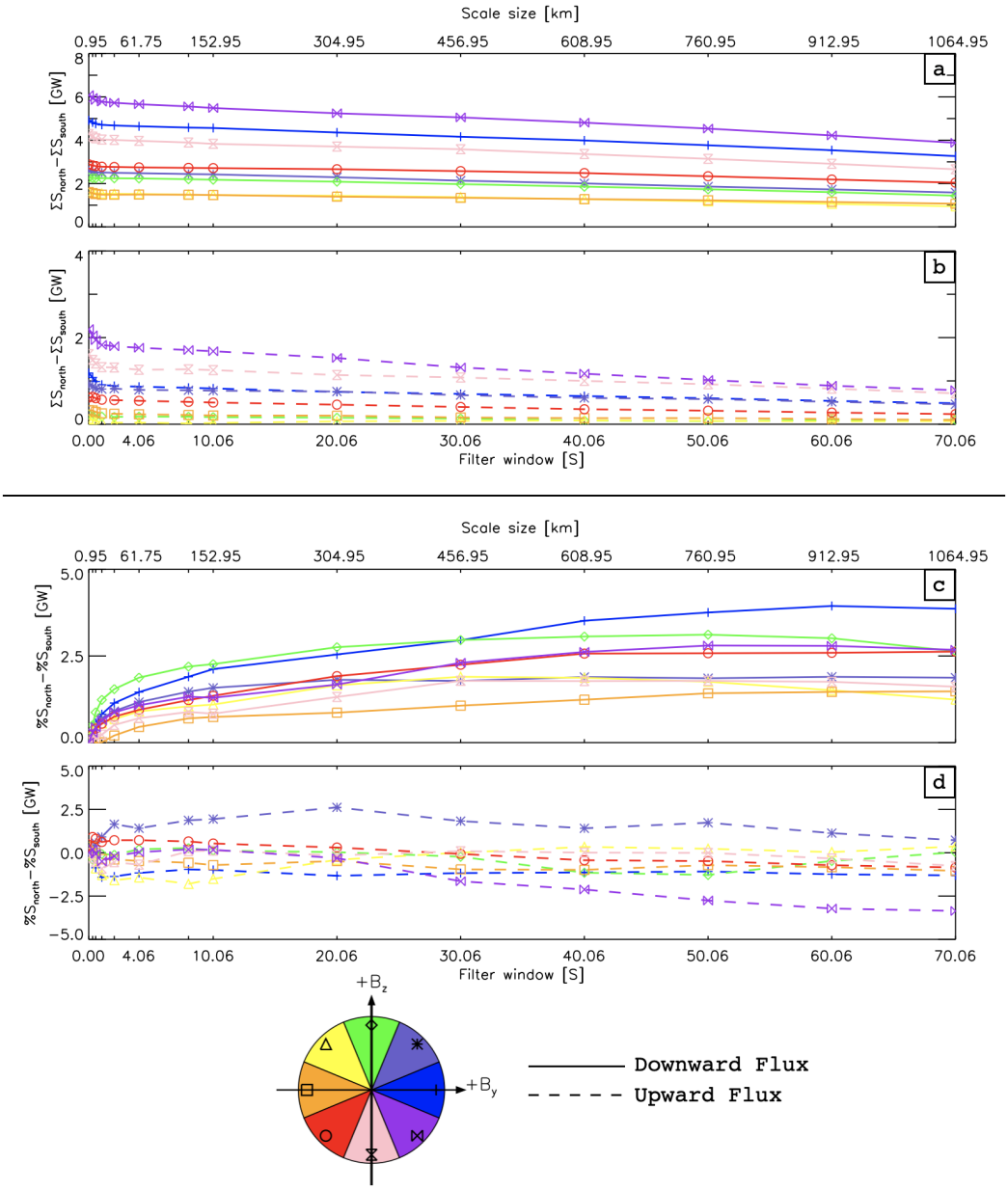

Figure 9. [a] and [b]: Difference between northern and southern hemispheric integrated Poynting flux magnitude with increasing SGLP filter size (southern subtracted from northern) for downward and upward Poynting flux, respectively. [c] and [d]: Difference between the percentage of initial unfiltered integrated Poynting flux. Colours, symbols and linestyles are the same as that in Figure 6.

power in the northern hemisphere, which holds true for all IMF orientations and SGLP filter sizes.

The main region responsible for the northern hemisphere integrated Poynting flux preference appears to be the dayside, as seen in Figure 8. Although the convection electric field asymmetries with IMF B_y can explain the pre/post-noon asymmetries, it does not explain the magnitude dominance of the northern hemisphere Poynting flux. Knipp et al. (2021) notes that the northern hemisphere experiences a greater amount of solar illumination and therefore conductivity, leading to a generally increased magnitude of field-aligned currents. Due to the intrinsically coupled nature of field-aligned currents and the dissipation of Poynting flux, this is likely a good reason for the hemispheric asymmetry seen in ours and other studies. Cosgrove et al. (2022) in turn note that this ultimately is probably because of geomagnetic field asymmetries between the two hemispheres.

In Figure 9[a] and [b], we see that the larger north-south differences in integrated Poynting flux typically occur during negative IMF B_z orientations, but also significantly during the purely B_y positive orientation (blue plus signs). Conversely, the integrated Poynting fluxes are closest for purely B_y negative orientations (orange squares). In Knipp et al. (2021), it was estimated that there was an approximate 25% increased Poynting flux in the northern hemisphere compared to the southern. We expand on the granularity of this estimation by observing a 1.5 GW/9% higher northern hemisphere integrated Poynting flux for purely B_y negative IMF orientations, and a 5 GW/28% higher value for B_y positive orientations. These estimations are for the unfiltered, 16 Hz Swarm statistics. From Figure 9[a] and [b], we also see that the difference in integrated values becomes smaller at larger SGLP filters. This narrowing of the lines implies that the driver of the north-south Poynting flux asymmetry has a greater impact at smaller spatial scales versus larger. If that driver is indeed the increased occurrence of small-scale Alfvénic field-aligned currents, then it makes sense that the asymmetry would be intensified with decreasing spatial scale.

Figure 9[c] and [d] display differences in the northern and southern hemisphere integrated Poynting flux, as a percentage of the unfiltered 16 Hz dataset (i.e. Figure 6b with the southern hemisphere values subtracted). In these plots, positive values mean that Poynting flux has decreased by a higher percentage from the initial integrated value in the southern hemisphere at the respective SGLP filter size, and vice versa for negative values. For the downward Poynting flux in Figure 9[c], the difference of percentages are consistently positive and also increase with SGLP filter size. This indicates that a

consistently higher percentage of downward Poynting flux is lost compared to unfiltered value in the southern hemisphere at all spatial scales, compared with the north. In other words, downward Poynting flux in the southern hemisphere decreases at a faster rate than in the north, although it is a significantly lower magnitude. For the upward Poynting flux in Figure 9[d], the relationship is much less clear. Figure 9[d] implies that upward Poynting flux in the northern and southern hemisphere decrease at comparable rates, with some IMF orientations potentially resulting in the hemispheric power loss being greater in one hemisphere or the other.

4 Summary

Using approximately 7 years of the newly reprocessed 16 Hz Swarm ion velocity dataset, along with magnetic field measurements from the onboard magnetometer, we have quantified the level at which Poynting flux in the MIT system is underestimated at larger spatial scales. We determine statistical patterns of the Poynting flux for both hemispheres and 8 IMF orientations, for 13 unique versions of the same dataset that have undergone varying Savitsky-Golay low-pass filters. The filtered datasets represent varying degrees of spatial scale over which the data is "smoothed", thus acting as a proxy for coarser and larger scale measurements. We note several key results from this analysis:

- Downward (into the ionosphere) and upward (out of) Poynting flux decreases with increasing scale size of observation. Compared to the unfiltered data (a scale size of 0.95 km), integrated Poynting flux decreases by as much as 5% and 15% for downward and upward Poynting flux respectively, when the scale size is increased to 8.55 km (roughly 2 Hz equivalent).
- At very small spatial scales, the drop in Poynting flux with increasing spatial scale is faster than at larger scales, where it becomes more linear.
- At the largest spatial scale tested (1064.95 km), both upward and downward Poynting flux is measured to be approximately half of the unfiltered equivalent.
- The spatial morphology of Poynting flux does not change significantly with increasing measurement scale, only the magnitudes, for all IMF orientations. A dayside cusp enhancement region appears to be an ever-present feature.
- The orientation of the IMF does not appear to drastically change the rate at which the measured Poynting flux decreases with increasing spatial scale. Northward IMF

orientations however result in consistently lower hemispherically integrated Poynting flux at all scales compared to southward orientations.

- Hemispherically integrated Poynting flux is 9-28% larger in the northern hemisphere than in the south, depending on IMF orientation. This follows from similar results by Pakhotin et al. (2021), Knipp et al. (2021) and Cosgrove et al. (2022).
- Downward Poynting flux decreases with spatial scale faster in the southern hemisphere than in the north. The relationship for upward Poynting flux is not clear from our results, but may be comparable for each hemisphere.

These results stress the importance of small-scale electric field variability, likely Alfvénic of origin, in driving a significant proportion of the MIT energy budget. Additionally, they show the need for caution when utilising datasets with a coarse or low-resolution spatio-temporal sampling rate. For example, the fitted data products of the Super Dual Auroral Radar Network (SuperDARN) and Active Magnetosphere and Planetary Electrodynamics Response Experiment (AMPERE) are not well suited for observing variability on scales much smaller than a few hundred kilometres. Larger scale science campaigns such as those, however, could be very well suited for capturing larger-scale, quasi-static Poynting fluxes, which are less impacted by Alfvén wave dynamics.

Acknowledgments

This research was supported by the European Space Agency (ESA) Living Planet Fellowship programme and by the National Sciences and Engineering Research Council of Canada (NSERC). DDB was supported by ESA under the "HLPF-SSA" project and by NSERC under CREATE Grant #479771-20. KM was supported by NSERC Discovery Grant #RGPIN 05472-2017. IPP was supported by a ESA DISC grant. Thermal Ion Imager (TII) data processing and calibration are supported at the University of Calgary via Canadian Space Agency Grant 15SUSWARM. 16 Hz TII data from the ESA Swarm A and B satellites was obtained from `https://swarm-diss.eo.esa.int`, in the "`Advanced/Plasma_Data/16_Hz_TIII_Cross-track_Dataset/New_baseline`" directory. 50 Hz high-res magnetic field measurements were obtained from the "`Level1b/Latest_baselines/MAGx_HR`" directory.

References

Anderson, B., Korth, H., Waters, C. L., Green, D. L., Merkin, V. G., Barnes, R. J., & Dyrud, L. P. (2014). Development of large-scale Birkeland currents determined from the Active Magnetosphere and Planetary Electrodynamics Response Experiment. *Geophysical Research Letters*, *41*(9), 3017–3025.

Billett, D. D., McWilliams, K. A., Perry, G. W., Clausen, L. B. N., & Anderson, B. J. (2022). Ionospheric energy input in response to changes in solar wind driving: Statistics from the SuperDARN and AMPERE campaigns. *Journal of Geophysical Research: Space Physics*, e2021JA030102.

Billett, D. D., Perry, G. W., Clausen, L. B. N., Archer, W. E., McWilliams, K. A., Haaland, S., ... others (2021). The relationship between large scale thermospheric density enhancements and the spatial distribution of Poynting flux. *Journal of Geophysical Research: Space Physics*, *126*(5), e2021JA029205.

Chaston, C. C., Carlson, C. W., McFadden, J. P., Ergun, R. E., & Strangeway, R. J. (2007). How important are dispersive Alfvén waves for auroral particle acceleration? *Geophysical Research Letters*, *34*(7).

Chisham, G., Lester, M., Milan, S. E., Freeman, M. P., Bristow, W. A., Grocott, A., ... others (2007). A decade of the Super Dual Auroral Radar Network (SuperDARN): Scientific achievements, new techniques and future directions. *Surveys in geophysics*, *28*(1), 33–109.

Codrescu, M. V., Fuller-Rowell, T. J., & Foster, J. C. (1995). On the importance of E-field variability for Joule heating in the high-latitude thermosphere. *Geophysical Research Letters*, *22*(17), 2393–2396.

Cosgrove, R. B., Bahcivan, H., Chen, S., Sanchez, E., & Knipp, D. (2022). Violation of Hemispheric Symmetry in Integrated Poynting Flux via an Empirical Model. *Geophysical Research Letters*, *49*(4), e2021GL097329.

Cosgrove, R. B., Bahcivan, H., Chen, S., Strangeway, R. J., Ortega, J., Alhassan, M., ... others (2014). Empirical model of Poynting flux derived from FAST data and a cusp signature. *Journal of Geophysical Research: Space Physics*, *119*(1), 411–430.

Cosgrove, R. B., & Codrescu, M. (2009). Electric field variability and model uncertainty: A classification of source terms in estimating the squared electric field from an electric field model. *Journal of Geophysical Research: Space Physics*,

114(A6).

Cousins, E. D. P., & Shepherd, S. G. (2010). A dynamical model of high-latitude convection derived from SuperDARN plasma drift measurements. *Journal of Geophysical Research: Space Physics*, *115*(A12).

Cousins, E. D. P., & Shepherd, S. G. (2012). Statistical characteristics of small-scale spatial and temporal electric field variability in the high-latitude ionosphere. *Journal of Geophysical Research: Space Physics*, *117*(A3).

Deng, Y., Fuller-Rowell, T. J., Akmaev, R. A., & Ridley, A. J. (2011). Impact of the altitudinal Joule heating distribution on the thermosphere. *Journal of Geophysical Research: Space Physics*, *116*(A5).

Förster, M., & Haaland, S. (2015). Interhemispheric differences in ionospheric convection: Cluster EDI observations revisited. *Journal of Geophysical Research: Space Physics*, *120*(7), 5805–5823.

Friis-Christensen, E., Lühr, H., & Hulot, G. (2006). Swarm: A constellation to study the Earth's magnetic field. *Earth, planets and space*, *58*(4), 351–358.

Gary, J. B., Heelis, R. A., & Thayer, J. P. (1995). Summary of field-aligned Poynting flux observations from DE 2. *Geophysical research letters*, *22*(14), 1861–1864.

Hatch, S. M., LaBelle, J., Lotko, W., Chaston, C. C., & Zhang, B. (2017). IMF control of Alfvénic energy transport and deposition at high latitudes. *Journal of Geophysical Research: Space Physics*, *122*(12), 12–189.

Hogan, B., Lotko, W., & Pham, K. (2020). Alfvénic thermospheric upwelling in a global geospace model. *Journal of Geophysical Research: Space Physics*, *125*(12), e2020JA028059.

Iijima, T., & Potemra, T. A. (1976). The amplitude distribution of field-aligned currents at northern high latitudes observed by Triad. *Journal of Geophysical Research*, *81*(13), 2165–2174.

Ivarsen, M. F., Park, J., Kwak, Y.-S., Jin, Y., Knudsen, D. J., & Clausen, L. B. N. (2020). Observational evidence for the role of Hall conductance in Alfvén wave reflection. *Journal of Geophysical Research: Space Physics*, *125*(12), e2020JA028119.

Keiling, A. (2021). The dynamics of the Alfvénic oval. *Journal of Atmospheric and Solar-Terrestrial Physics*, *219*, 105616.

Keiling, A., Wygant, J. R., Cattell, C. A., Mozer, F. S., & Russell, C. T. (2003). The global morphology of wave Poynting flux: Powering the aurora. *Science*, *299*(5605), 383–386.

Kelley, M. C., Knudsen, D. J., & Vickrey, J. F. (1991). Poynting flux measurements on a satellite: A diagnostic tool for space research. *Journal of Geophysical Research: Space Physics*, *96*(A1), 201–207.

Knipp, D., Kilcommons, L., Hairston, M., & Coley, W. R. (2021). Hemispheric asymmetries in Poynting flux derived from DMSP spacecraft. *Geophysical Research Letters*, *48*(17), e2021GL094781.

Knudsen, D. J. (1990). *Alfvén waves and static fields in magnetosphere/ionosphere coupling: In-situ measurements and a numerical model*. Cornell University, August.

Knudsen, D. J., Burchill, J. K., Buchert, S. C., Eriksson, A., Gill, R., Wahlund, J.-E., ... Moffat, B. (2017). Thermal ion imagers and Langmuir probes in the Swarm electric field instruments. *Journal of Geophysical Research: Space Physics*, *122*(2), 2655–2673.

Knudsen, D. J., Kelley, M. C., & Vickrey, J. F. (1992). Alfvén waves in the auroral ionosphere: A numerical model compared with measurements. *Journal of Geophysical Research: Space Physics*, *97*(A1), 77–90.

Koustov, A. V., Lavoie, D. B., Kouznetsov, A. F., Burchill, J. K., Knudsen, D. J., & Fiori, R. A. D. (2019). A comparison of cross-track ion drift measured by the Swarm satellites and plasma convection velocity measured by SuperDARN. *Journal of Geophysical Research: Space Physics*, *124*(6), 4710–4724.

Leger, J.-M., Bertrand, F., Jager, T., Le Prado, M., Fratter, I., & Lalaurie, J.-C. (2009). Swarm absolute scalar and vector magnetometer based on helium 4 optical pumping. *Procedia Chemistry*, *1*(1), 634–637.

Lomidze, L., Burchill, J. K., Knudsen, D. J., Kouznetsov, A., & Weimer, D. R. (2019). Validity Study of the Swarm Horizontal Cross-Track Ion Drift Velocities in the High-Latitude Ionosphere. *Earth and Space Science*, *6*(3), 411-432. Retrieved from `https://agupubs.onlinelibrary.wiley.com/doi/abs/10.1029/2018EA000546` doi: https://doi.org/10.1029/2018EA000546

Lotko, W., & Zhang, B. (2018). Alfvénic heating in the cusp ionosphere-thermosphere. *Journal of Geophysical Research: Space Physics*, *123*(12),

10–368.

Lühr, H., Park, J., Gjerloev, J. W., Rauberg, J., Michaelis, I., Merayo, J. M. G., & Brauer, P. (2015). Field-aligned currents' scale analysis performed with the Swarm constellation. *Geophysical Research Letters*, *42*(1), 1–8.

Lühr, H., Rother, M., Köhler, W., Ritter, P., & Grunwaldt, L. (2004). Thermospheric up-welling in the cusp region: Evidence from CHAMP observations. *Geophysical Research Letters*, *31*(6).

Matsuo, T., & Richmond, A. D. (2008). Effects of high-latitude ionospheric electric field variability on global thermospheric Joule heating and mechanical energy transfer rate. *Journal of Geophysical Research: Space Physics*, *113*(A7).

Miles, D. M., Mann, I. R., Pakhotin, I. P., Burchill, J. K., Howarth, A. D., Knudsen, D. J., ... Yau, A. W. (2018). Alfvénic dynamics and fine structuring of discrete auroral arcs: Swarm and e-POP observations. *Geophysical Research Letters*, *45*(2), 545–555.

Olsson, A., Janhunen, P., Karlsson, T., Ivchenko, N., & Blomberg, L. G. (2004). Statistics of Joule heating in the auroral zone and polar cap using Astrid-2 satellite Poynting flux. In *Annales geophysicae* (Vol. 22, pp. 4133–4142).

Pakhotin, I. P., Mann, I. R., Lysak, R. L., Knudsen, D. J., Gjerloev, J. W., Rae, I. J., ... others (2018). Diagnosing the role of Alfvén waves in magnetosphere-ionosphere coupling: Swarm observations of large amplitude nonstationary magnetic perturbations during an interval of northward IMF. *Journal of Geophysical Research: Space Physics*, *123*(1), 326–340.

Pakhotin, I. P., Mann, I. R., Xie, K., Burchill, J. K., & Knudsen, D. J. (2021). Northern preference for terrestrial electromagnetic energy input from space weather. *Nature communications*, *12*(1), 1–9.

Park, J., Lühr, H., Knudsen, D. J., Burchill, J. K., & Kwak, Y.-S. (2017). Alfvén waves in the auroral region, their Poynting flux, and reflection coefficient as estimated from Swarm observations. *Journal of Geophysical Research: Space Physics*, *122*(2), 2345–2360.

Pettigrew, E. D., Shepherd, S. G., & Ruohoniemi, J. M. (2010). Climatological patterns of high-latitude convection in the Northern and Southern hemispheres: Dipole tilt dependencies and interhemispheric comparisons. *Journal of Geophysical Research: Space Physics*, *115*(A7).

Ruohoniemi, J. M., & Greenwald, R. A. (1996). Statistical patterns of high-latitude convection obtained from Goose Bay HF radar observations. *Journal of Geophysical Research: Space Physics*, *101*(A10), 21743–21763.

Shepherd, S. G. (2014). Altitude-adjusted corrected geomagnetic coordinates: Definition and functional approximations. *Journal of Geophysical Research: Space Physics*, *119*(9), 7501–7521.

Thomas, E. G., & Shepherd, S. G. (2018). Statistical patterns of ionospheric convection derived from mid-latitude, high-latitude, and polar SuperDARN HF radar observations. *Journal of Geophysical Research: Space Physics*, *123*(4), 3196–3216.

Weimer, D. R. (2005). Improved ionospheric electrodynamic models and application to calculating Joule heating rates. *Journal of Geophysical Research: Space Physics*, *110*(A5).

Zhang, B., Lotko, W., Brambles, O., Xi, S., Wiltberger, M., & Lyon, J. (2014). Solar wind control of auroral Alfvénic power generated in the magnetotail. *Journal of Geophysical Research: Space Physics*, *119*(3), 1734–1748.